Vapor–liquid equilibria and heat effects of hydrogen fluoride from molecular simulation

Donald P. Visco, Jr. and David A. Kofke
Department of Chemical Engineering, State University of New York at Buffalo, Buffalo, New York 14260

(Received 19 March 1998; accepted 2 June 1998)

The vapor–liquid coexistence densities, vapor pressure, and heat of vaporization of hydrogen fluoride (HF) is calculated via Monte Carlo simulation from three intermolecular potential models that are found in the literature. The first is a pure pair potential based solely on *ab initio* data, the second is a semi-empirical pair potential which uses an *ab initio* derived surface fitted with dimer spectroscopic data, and the third is an *effective* pair potential that was fit to experimental data for the condensed phase. As expected, the effective potential reproduces the saturated liquid densities more accurately than the others do, while all the potential models predict the wrong slope and curvature in the vapor pressure curve. The inability to reproduce the vapor pressure dependence on temperature is connected to the models' poor prediction of the heat of vaporization at temperatures below 400 K. A biasing algorithm is introduced to study the superheated-vapor heat capacity, density, association number, and oligomer distribution along three low-pressure isobars using both the semi-empirical and effective pair potentials. It is found that both these potential models do predict a peak in the heat capacity, however, they are at cooler temperatures and only about half the magnitude relative to the experiment. When comparing the potential models to each other, it is found that the semi-empirical pair potential predicts the onset of near-ideal gas conditions at about 30 K cooler than the effective pair potential. Additionally, the percentage of ring oligomers predicted by both models is considerable at all but the highest temperatures. Both models also agree that the monomer and cyclic tetramer are the two most important species at the nonideal states. [S0021-9606(98)50134-1]

I. INTRODUCTION

Hydrogen fluoride (HF) has enjoyed renewed importance, in part because it is a raw material in the production of hydrofluorocarbons (HFCs), which are now used as replacement refrigerants for chlorofluorocarbons (CFCs). While there has been a substantial increase in the number of published experiments on HFC systems,[1–8] surprisingly few new results have been reported for HF+HFC systems,[9] and none have been published recently on pure HF. A likely reason that data for HF-containing systems have not been forthcoming is due to the highly caustic and toxic nature of hydrogen fluoride.

Instead, there has been a rise in the number of equations of state (EOS) developed specifically for HF with clear extensions to include HFCs (as inerts).[10–14] Most of these HF engineering models combine a conventional cubic EOS with an association model that describes the formation of hydrogen-bonded HF oligomers through the use of reaction equilibria constants. The choice and distribution of the oligomers used in the association schemes for these and other models have varied widely. A common, simple scheme based partly on spectroscopic evidence[15] and electron diffraction[16] studies assumes a monomer–hexamer model for HF association with no distinction between the chain or ring or branched hexamer. Others have included the dimer and/or trimer and/or tetramer in addition to the monomer and hexamer.[17] The exclusion of the pentamer seems to be unfounded as new evidence has revealed that this oligomer is present.[18] Still another model has chosen to include all oligomers with a Poisson-like distribution that promotes the formation of hexamers.[10] While these efforts have met with varying degrees of success, their performance is affected by many factors, only one of which is the choice of association scheme. Consequently it is difficult to draw conclusions about the truth of a given association scheme solely from the performance of a model built upon it.

Separate from these chemical models of HF is the statistical associating fluid theory (SAFT) approach,[19] which introduces a more detailed picture of the statistical mechanics of association. SAFT is built upon a molecular model, and does not require an explicit association scheme as input. Application of SAFT to HF has been attempted only recently,[14] and further development is under way. The present implementations have done reasonably well in describing vapor pressure, but have been found deficient in characterizing heat effects.[20] This shortcoming points to an inadequate description of association and, as with the chemical models, this problem can be overcome most effectively by improving our molecular picture of these phenomena.

The HF dimer contains only 20 electrons making it quite amenable to an *ab initio* study of hydrogen bonding, more so than other strongly associating systems such as hydrogen chloride or water. The usual route is to determine a dimer potential energy surface (PES) at some level of theory and fit the results onto an analytic description of the surface. These equations are then used to extract various spectroscopic con-

stants of interest to the investigator. These analytic descriptions of the dimer PES can be used in molecular dynamics (MD) or Monte Carlo (MC) simulations to predict transport or thermodynamic properties of HF. Since this is specifically a two-body potential, one can compare the results with experimental data and estimate the importance of 3+ body effects for various quantities, to the extent that the PES is accurate.

Quite distinct from the ''true'' pair-wise potentials developed via *ab initio* studies of HF are *effective* pair potentials. These are usually based on condensed-phase data where the 3+ body effects are absorbed into the parameters of the potential model. Typically a limited set of thermodynamic properties (e.g., liquid density, enthalpy) are used to establish the model parameters, and it is not unusual to find that other properties are not predicted with the same level of accuracy (although the results are usually better than those obtained from a purely *ab initio* potential).

Of particular interest for HF is the oligomer distribution, because this is something that molecular simulation is uniquely positioned to provide and because the clustering behavior has a profound effect on HF thermodynamic properties. A good quantitative understanding of clustering can guide engineering model development. However one has no assurance that oligomer distributions measured in simulation are true—the parameters of effective potentials cannot be expected to yield these distributions accurately because they are not fit to this property, which is for the most part experimentally inaccessible. Instead *ab initio* models that account for higher than pair interactions may be the only alternative. Thus a viable route to the development of an effective potential that accurately characterizes clustering might involve verification against such high-quality *ab initio* studies. Experimentally the heat capacity, particularly in the vapor, provides a (limited) view of the clustering behavior. The vapor-phase heat capacity is marked by a sharp peak that seems to be connected to the formation of HF oligomers. A molecular model that purports to describe the clustering behavior correctly should present heat capacities that are in quantitative agreement with this observation.

The history of the computer simulation of HF began about 2 decades ago with an MD study of the liquid by Klein *et al.*[21] who reported diffusion coefficients, internal energies, and radial distribution functions (RDFs). Since that time there have been several MD and MC simulations performed on the liquid. The variations in these simulations include the development and use of different potential models,[22–26] the explicit inclusion of polarizability,[27,28] and the inclusion of corrections for the long ranged Coulombic interactions.[29] Additionally, Car–Parrinello *ab initio* MD simulations have been performed on the pure liquid[30] and a dilute aqueous solution.[31] Most researchers report internal energies and RDFs with some including heat capacity results or oligomer information on the liquid. Simulations of HF vapor were done on clusters of various sizes[32,33] from which the entropy and energy change as a function of cluster size is reported. No simulations currently exist for HF in the two-phase region nor for the heat capacity of the superheated vapor.

The Metropolis Monte Carlo simulation method is designed to sample the Boltzmann distribution of an ensemble.[34] Unfortunately, there are situations where one cannot, at least during a simulation of reasonable length, sample configurations according to this distribution. Nonergodicity may arise in potential models, like HF, that need to be directionally dependent with steep, narrow wells that attempt to describe association. During the course of a simulation, however, these steep, narrow wells tend to trap the simulation into a small, confined area of configuration space. Opposite to this and just as debilitating, is the problem that the simulation never explores these low-energy configurations because it does not happen upon them. An efficient, effective simulation of associating systems needs to be aware of and account for these complimentary problematic situations.

For this study, we determine the vapor–liquid equilibria (VLE), vapor pressure, and heat of vaporization from three potential models: one ''true'' pair potential, one semi-empirical pair potential, and one effective pair potential. Additionally, we look at the volumetric behavior, oligomer distribution, and constant-pressure heat capacity predicted by the semi-empirical and effective pair potentials at some superheated-vapor states. This article is organized as follows. In Sec. II we describe molecular simulation techniques used to determine the VLE properties, review the model potentials examined in this study, and discuss how vapor-phase heat capacities are measured, with a brief description of a biasing method used to enhance the sampling of configurations. In Secs. III and IV we present the VLE and superheated-vapor results, respectively. Section V presents concluding remarks.

II. POTENTIALS AND METHODS

In this section we give details of the VLE and heat of vaporization study. First, each of the models will be given a cursory description; the reader is referred to the specific paper in which these models first appeared for more detail.

A. Potential models

1. W. L. Jorgensen, 1979 (J79)

The energy for this potential[23] is given by

$$u_{i,j}=\sum_{Vi}\sum_{Wj}(q_{Vi}q_{Wj}/r_{Vi,Wj}) + \sum_{Si}\sum_{Tj}\left(\frac{b_{\mathrm{ST}}}{r_{Si,Tj}^{3}}+\frac{c_{\mathrm{ST}}}{r_{Si,Tj}^{6}}+\frac{d_{\mathrm{ST}}}{r_{Si,Tj}^{12}}\right), \tag{1}$$

where i and j are HF molecules, q_{Vi} is the charge of site V on molecule i, q_{Wi} is the charge of site W on molecule j, $r_{Vi,Wj}$ is the distance between sites V on molecule i and W on molecule j, the atom parameters are b,c,d with the subscripts indicating the type of atom, $r_{Si,Tj}$ is the distance between atoms S on molecule i and T on molecule j; these parameters are recorded in Table I.

This pair potential is based on dimer energies calculated from an STO-3G basis set with the HF bond length held fixed at 0.917 Å. This is a three-site model with charges on the fluorine and hydrogen atom centers. The neutralizing

TABLE I. Potential parameters for J79.[a] The parameters correspond to energy in kcal/mol.

	Parameter		
	FF	FH	HH
b	50.4631	−56.4092	62.3553
c	−153.412	10.0910	−85.1490
d	61101.7	486.416	1521.03
	q_F	$q_{neutral}$	q_H
	−14.794	−9.153	−5.641

[a]See Ref. 23.

charge is placed 0.416 Å from the F atom away from the H atom along the bond axis. The spherical cutoff radius has been specified as 7.6166 Å and, as the potential was developed without any long-range correction for truncation, no such corrections were applied.

2. A. E. Barton and B. J. Howard, 1982 (BH82)

This PES is based on the form derived from the *ab initio* work of Yarkony and co-workers[35] but is parameterized with molecular-beam spectroscopic data for the dimer. The pair potential is given explicitly in terms of four variables: the distance between the center of mass of the two molecules; the two angles between the line connecting the centers of mass and each bond axis; and the dihedral angle. Exponential terms are used to capture the repulsion in the potential while the classical electrostatic interaction is given in terms of spherical harmonics.[24] We chose a cutoff radius of 9.5 Å, and included long-range corrections in terms of orientationally averaged dipole–dipole, dipole–quadrupole, and quadrupole–quadrupole energies.[36]

3. M. E. Cournoyer and W. L. Jorgensen, 1984 (CJ84)

The interaction energy for this potential[26] is given by

$$u_{i,j}=\sum_{Vi}\sum_{Wj}(q_{Vi}q_{Wj}e^2/r_{Vi,Wj})+Ar_{FF}^{-12}-Cr_{FF}^{-6}, \qquad (2)$$

where i and j are two monomers, q_{Vi} is the charge of site V on molecule i, q_{Wj} is the charge of site W on molecule j, $r_{Vi,Wj}$ is the distance between sites V on molecule i and W on molecule j, e is the electrostatic charge, and A and C are Lennard-Jones (LJ) parameters.

This effective pair potential has parameters determined via MC iteration to liquid phase experimental data with a fixed HF bond length of 0.917 Å. This is a three-site model with a charge of $+0.725e$ on both the fluorine and hydrogen atom centers. The neutralizing charge is placed 0.166 Å from the F atom toward the H atom along the bond axis. The fitted parameters have values of $A=3.0\times10^5$ kcal Å^{12}/mol and $C=425$ kcal Å^6/mol. A spherical cutoff radius of 8.0 Å was used for all the simulations of this potential. Following Cournoyer and Jorgensen,[26] a long-range correction for only the LJ part of the potential was included for interactions beyond the cutoff.

B. Gibbs ensemble and Gibbs–Duhem integration parameters

For the VLE study, the Gibbs–Duhem integration (GDI) technique[37] was used from high to low temperatures with the initial state point obtained from a long Gibbs ensemble (GE) simulation.[38] The pressure from the GE simulations, used to initiate the GDI series, was calculated from the vapor virial for the J79 and CJ84 potentials. The pressure determined from the GE simulation of the BH82 potential, owing to its more complicated nature, was calculated through a method described in the Appendix.

Spherical cut-off was used in cubic boxes, and the cutoff radius is listed with the description of the potentials below. All cutoffs were determined with respect to fluorine–fluorine atom distance. During the GE simulations, the ratio of volume moves, displacement moves rotation moves, and particle exchange moves was $2{:}N{:}N{:}8N$, where N is the number of particles in the corresponding phase. Further simulation details are given in Table II.

C. Superheated vapor study

A superheated vapor study on the BH82 and CJ84 potential models was performed to determine the constant pressure heat capacity predicted via these models. Constant pressure–constant temperature (NPT) Monte Carlo simulations were done on 108 monomers with 5 million equilibration and 10 million production configurations. During these NPT simulations, the ratio of volume moves, displacement moves, and rotation moves were $5{:}2N{:}2N$. The heat capacity values reported are based on all the production configurations contributing to one value. The error bars are based on blocks of 1 million configurations. (All error bars for all averages in this work are ±1 standard deviation of the reported mean.)

Since the calculation of fluctuation properties is especially sensitive to the exploration of configuration space, before going further we should explore the question of whether sampling problems prevent us from measuring the heat capacity for these two models. In Fig. 1 we show the energy

TABLE II. Simulation parameters for the Gibbs ensemble and Gibbs–Duhem integration runs for each potential model (configurations=Cfgs, iteration=Iter).

	GE			GDI						
Model	N	Equil Cfgs	Prod Cfgs	N_{liq}	N_{vap}	Pred Iters	Cfgs Pred Iter	Corr Iters	Cfgs Corr Iter	Prod Cfgs
J79	250	5 million	25 million	230	20	1	1 million	10	1 million	1.5 million
BH82	250	5 million	25 million	218	32	1	500 000	6	500 000	500 000
CJ84	250	5 million	25 million	225	25	1	1 million	10	1 million	1.5 million

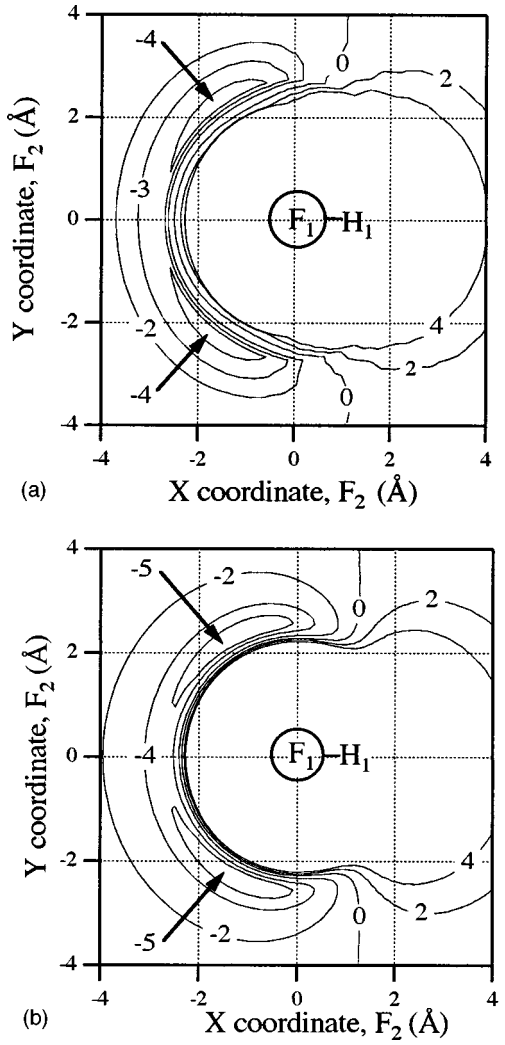

FIG. 1. Energy contours for two co-planar HF molecules from the BH82 potential model (a) and the CJ84 potential model (b). The contours are in units of kcal/mol.

contours between two planar HF molecules for the BH82 model (a) and the CJ84 model (b). These contours were created by first placing an F atom (F_1) of one molecule at the origin and making its H atom (H_1) lie on the positive X axis. Next, we rotated a second F atom (F_2) in circles of increasing radius centered at the origin with its H atom (H_2) pointing towards the origin (F_1). From both sets of contours, one can easily envision a scenario where the second HF molecule is caught in the potential well of the first molecule over the course of many configurations. Of course a simulation which does not sample the configurations in the potential wells is not extracting the correct thermodynamic information, *a fortiori* for fluctuation quantity calculations such as the heat capacity. Low density states are especially susceptible to this sampling problem.

One reasonable solution to this sampling problem is to run the simulation in a way that enables molecules to move in and out of potential wells with some regularity. Several such biasing methods have been suggested recently in the literature, some more complex than others. The easiest to implement[39] simply conducts particle movement on two scales: intermolecular and intramolecular. Others such as the

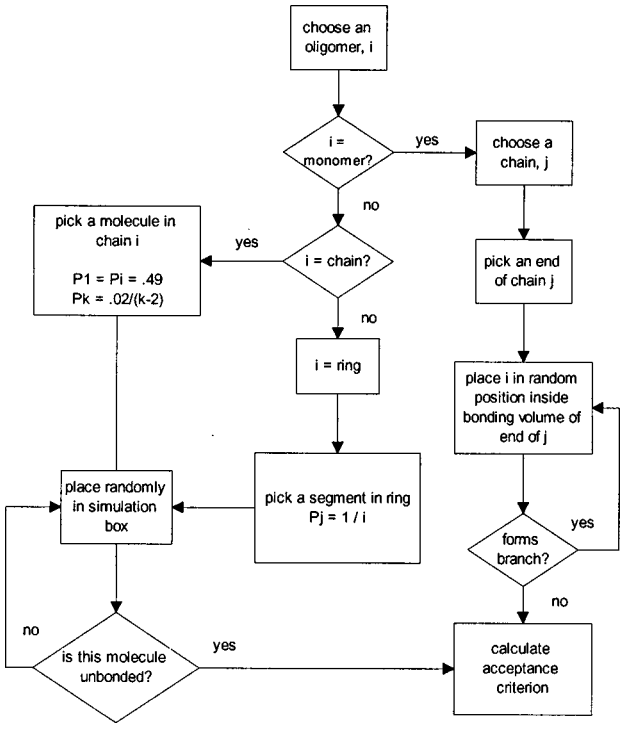

FIG. 2. A flowsheet showing the logical structure of the monomer addition-subtraction algorithm (MASA). To illustrate the types of acceptance criteria that are contained within this algorithm, we will walk through a step with the probabilities of each move in parenthesis. If a monomer A is chosen ($1/N_{\mathrm{tot}}$; N_{tot} is the total number of oligomers, both chains and rings), we next pick a chain B of length k ($1/(N_c-1)$; N_c is the total number of chains) and an end of chain B ($\frac{1}{2}$). Then we place the monomer in the bonding volume of the chosen end of B ($1/V_{\mathrm{eff}}$). From here, three things can occur. The first is that a chain of length $k+1$ is formed (one H bond). Second is that monomer A completes a ring of length $k+1$ (two H bonds). Third is that monomer A bridges two chains (two H bonds). Thus, for example, if the first scenario is encountered, the acceptance criteria for this move is $\min[1,2P_E(V_{\mathrm{eff}}/V)(N_{\mathrm{tot}})(N_c-1)/(N_{\mathrm{tot}}-1)\exp(-\beta\Delta U)]$ where P_E is the probability that a particular end of the chain is chosen (here it is 0.49; note that there is a finite probability of choosing a nonend molecule in a chain to satisfy detailed balance). Note also that for the reverse move where we place a molecule in an unbonded position (breaking a bond), the correct probability is $1/(V-NV_{\mathrm{eff}})$, yet at this low-density state $NV_{\mathrm{eff}}/V\sim10^{-3}$ thus we make the assumption that $(V-NV_{\mathrm{eff}})\sim V$.

association biased Monte Carlo[40] method of Busch *et al.* and the bond-bias Monte Carlo[41] method of Tsangaris and de Pablo biases the simulation so that bonding and unbonding moves are attempted more frequently than would be found using normal Metropolis moves; of course the bias so introduced is removed when deciding acceptance. The latter two, although more efficient than the former, are much more complicated to implement. We have chosen a middle ground approach that modifies the bond-bias algorithms in a way that leaves them less efficient yet less complicated to implement. We call our algorithm the monomer addition-subtraction algorithm (MASA). It should be noted that MASA prohibits the formation of branched oligomers as these species significantly complicate the algorithm. This is a valid assumption for the present study as we are using this algorithm only for the superheated vapor; at this low density state *ab initio* studies indicate that branching is unimportant.[42] The algorithm is summarized via a flow diagram in Fig. 2; further details and evaluation of this algorithm will be presented elsewhere.

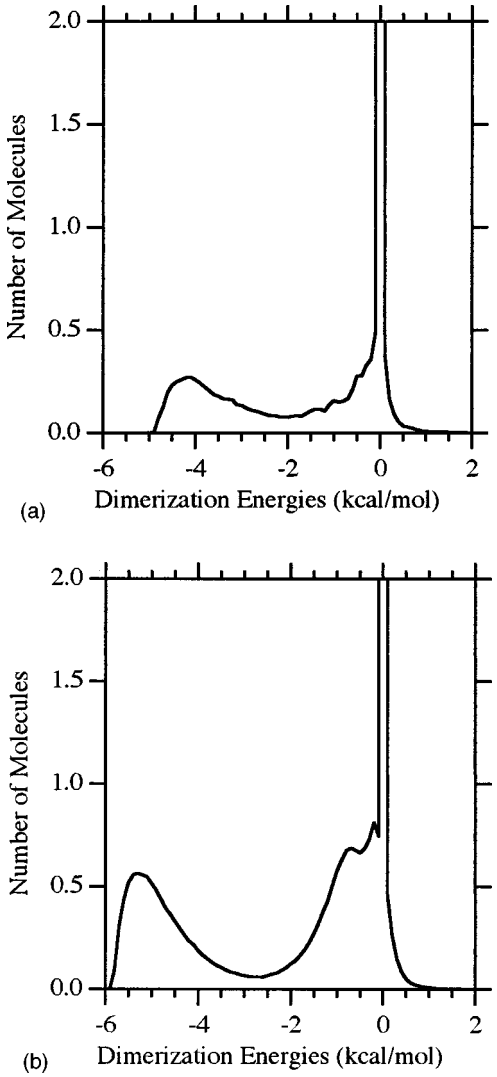

FIG. 3. A histogram of the number of molecules over a range of dimerization energies for the BH82 model (a) and the CJ84 model (b). The low energy peak is due to hydrogen bonding while the peak near 0 is due to interactions with the bulk.

The question of what constitutes the bonding volume for HF is nebulous at best. After the work of Cournoyer and Jorgensen,[26] we have used an energetic definition of the hydrogen bond. Figure 3 shows the energetics from NPT nonbiased simulations of the superheated vapor at 270 K and 96.1 kPa. Any interaction energy less than around -2 kcal/mol for BH82 (a) and -3 kcal/mol for CJ84 (b) can be attributed to the hydrogen bonding interactions (here and throughout this article we define all molar quantities on an ''apparent'' basis, which ignores any oligomer formation; that is, 1 mole=20.0064 g). With this definition, we can revisit the energy contours of Fig. 1 to associate the appropriate energy limits with bonding volumes for each model. For example, from Fig. 1(a), we can envision two hemispheres around F_1: one with an outer radius of 3.7 Å and a second with an inner radius of 2.6 Å which combined is a fair approximation of the -2 kcal/mol contour. We will rotate this area out of the plane to create a bonding volume which is a half shell. Since Fig. 1(a) is in terms of F–F distances, we simply subtract the bond length from the radii determined above to give a more useful F_1-H_2 distance for our bonding volume. The same procedure is used for the CJ84 potential.

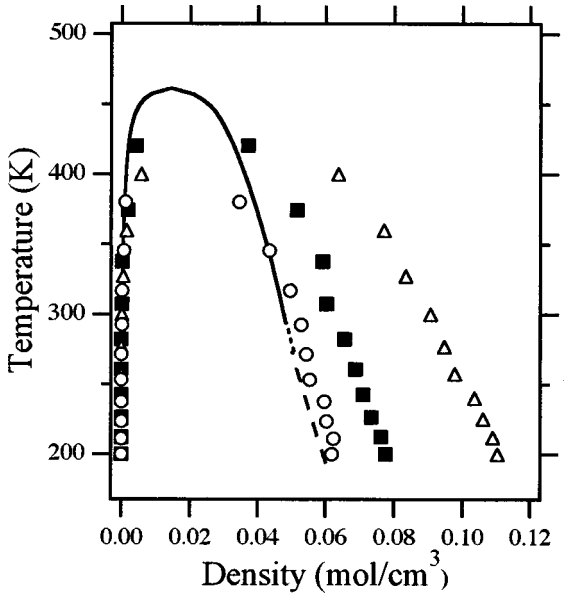

FIG. 4. Simulation coexistence densities as calculated from the potential models compared to experimental data. Symbols are as follows: open triangles (J79), filled squares (BH82), open circles (CJ84). Lines are as follows: solid line (Ref. 43), dotted line (Ref. 44), dashed line (Ref. 45). Confidence limits of the simulation data are smaller than their plotting symbols.

Armed with these definitions of bonding volumes, we have performed nonbiased and biased NPT simulations on the superheated vapor for the CJ84 potential at 96.1 kPa to explore the effects of adding the biased move. Additionally, we have performed biased NPT simulations at two other low-pressure states, 56.0 and 15.5 kPa on the CJ84 potential. We have also run biased NPT simulations for the superheated vapor on the BH82 potential along all three isobars mentioned above. For the biased simulations, we have included random particle insertions within a simulation box, in addition to the MASA move, to allow for large displacements of a molecule. During these biased NPT simulations, the ratio of volume moves, displacement moves, rotation moves, insertion moves, and MASA moves were $5{:}2N{:}2N{:}2N{:}15N$.

III. VLE RESULTS

Figure 4 shows the results of the VLE calculation as compared to published experimental data[43–45] while Fig. 5 focuses on the saturated vapor density. As expected, the effective pair potential compares favorably to experimental data relative to the other two-body potentials for the saturated liquid. That BH82 does a better job at the saturated liquid densities than does J79 may make one suspect that the exclusion of the long-range corrections to J79 is the culprit. However, we have studied this model with the inclusion of long-range corrections and have found no substantial change in the liquid density. Jorgensen had not included any long-range corrections in his constant volume–constant temperature simulations using this potential, and we wanted to keep as close as possible to his original work in our evaluation. The effective potential also does a good job on the vapor

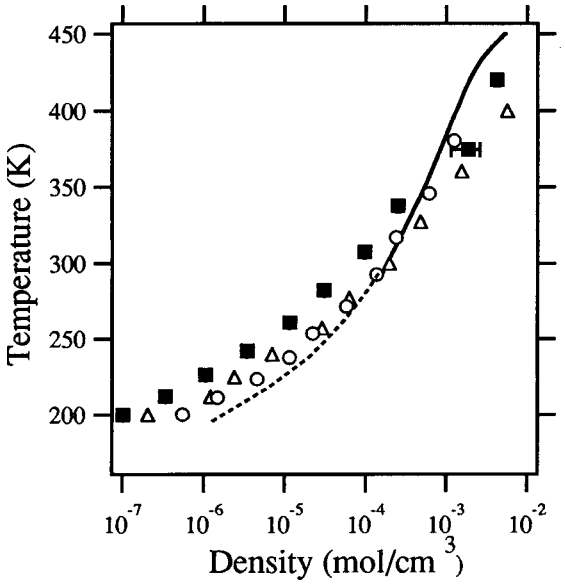

FIG. 5. Saturated vapor density as calculated from the potential models compared to experimental data. Symbols are as in Fig. 4. Lines are as follows: solid line (Ref. 43), dashed line (Ref. 12). Confidence limits of the simulation data are shown only where they are larger than the plotting symbol.

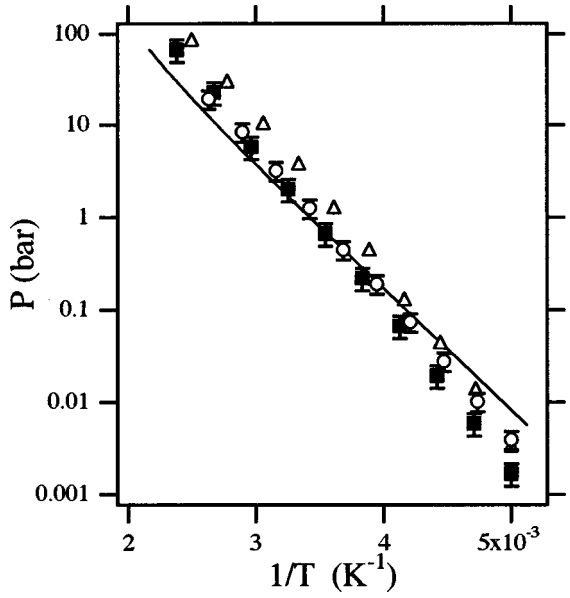

FIG. 6. The vapor pressure from the potential models as compared to experimental data. The experimental data are slightly concave up whereas all the simulation results are slightly concave down (best seen by looking along the curves from a point near the plane of the paper). Symbols are as in Figure 4. The line is the experimental data as obtained from Ref. 12. Confidence limits of the simulation data are shown only where they are larger than the plotting symbol.

densities. Clearly the implicit inclusion of the 3+ body interactions is important for the vapor as well, although few conclusions can be drawn from these data because of the large influence of the differing saturation pressures on the vapor densities. It is interesting to note that the CJ84 effective potential appears to predict a lower critical temperature than the other potentials, which puts it at odds with the experimental data. It seems the extrapolation of the effective potential to the high temperature and low density states underestimates the attraction at these states. At moderate temperatures it is noted that the two-body potentials overestimate the liquid density relative to the effective potential.

We look at the vapor pressure in Fig. 6. All of the models predict a higher value for the vapor pressure relative to experiment[12] at elevated temperatures, the two-body potentials being worse than the effective potential. All of the vapor pressure curves predicted by the models are concave down while the experimental vapor pressure curve is concave up. There is some region where the model curves and experimental curves cross. As seen in Fig. 7, this erroneous slope translates through the Clausius–Clapeyron equation to poor prediction of the heat of vaporization relative to experimental data.[43,46,47]

IV. SUPERHEATED VAPOR STUDY: RESULTS

In Fig. 8 we compare the results of the unbiased and biased NPT simulations of the CJ84 model at 96.1 kPa to experiment.[48] Both the unbiased and biased simulations predict the same peak in the heat capacity at around 290 K, but the biased simulations on the whole provide a much smoother curve than the unbiased simulations. Thus, it was concluded that the biased simulation, at least at this state, will allow for a more realistic determination of the heat capacities. Note that when comparing the biased and unbiased simulations for certain properties (density and internal energy), most of the results were the same [within ± 1 standard deviation of the mean (sdm)]. At the few states where this was not true, it was observed that very long unbiased simulations were tending in the direction of the biased results at that state. In Fig. 9 we compare the constant-pressure heat capacity of the BH82 model and the CJ84 model to that of the experiment at 96.1 kPa (a), 56.0 kPa (b), and 15.5 kPa

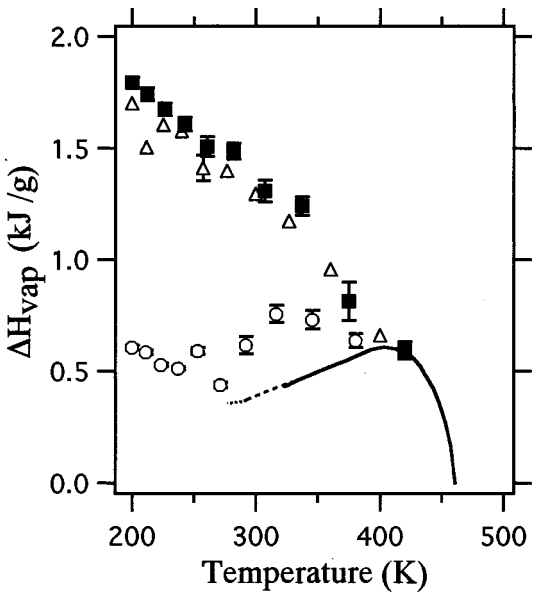

FIG. 7. The heat of vaporization as calculated from the potential models compared to experimental data. Symbols are as in Fig. 4. Lines are as follows: solid line (Ref. 43), dotted line (Ref. 46), dashed line (Ref. 47). Confidence limits of the simulation data are shown only where they are larger than the plotting symbol.

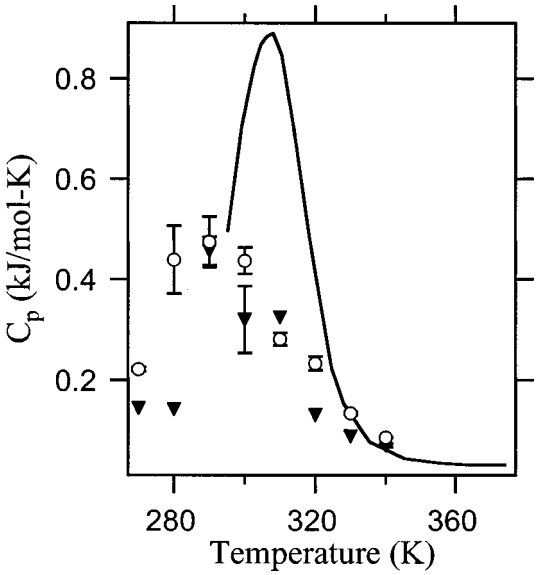

FIG. 8. The heat capacity of the superheated vapor at 96.1 kPa as calculated from biased (open circles) and non-biased (filled triangles) NPT simulations from the CJ84 potential model compared to the experimental data of Ref. 48 (line). Confidence limits of the simulation data are shown only where they are larger than the plotting symbol.

(c). Both models underestimate the peak in the heat capacity by about half for all three pressures tested. Additionally, simulation shows that for both models the heat capacity peaks occur at temperatures lower than the experiment. Comparing the simulation results to each other, it is observed that the semi-empirical pair potential yields a peak at 30–40 K cooler than the effective potential. To explore the reasons behind this, it is necessary to look at the densities predicted by both models at the same state. In Fig. 10 we show the superheated vapor densities and compare them to experiment at states where data exist. For a given temperature, experiment indicates a more dense vapor than either of the potential models. Comparing the two models to each other, the effective potential provides a larger density than the semi-empirical model at a given state. The effect of the poor prediction of the density by these potential models is seen in Fig. 11 which looks at the association number versus temperature along the three isobars. The association number is defined as the ratio of the number of HF molecules to the number of oligomers. Experimental values of the association number can be estimated by assuming an ideal gas of oligomers. The degree of association predicted by the potential models is less than that predicted by the experiment. The rise in association number has the character of a phase transition, and is therefore strongly connected to the peak in the heat capacity. One may postulate that better reproduction of the experimental superheated vapor density will aid in capturing the temperature at which the peak in the heat capacity occurs, with the height of the peak being a separate issue, explored next.

An interesting question arises, however, if we examine the association number that coincides with the heat capacity peak for both potentials and experiment. From Table III we see that for the 96.1 kPa isobar all methods predict a similar value of the association number at the heat capacity peak. A brief review of the terms that make up the heat capacity for a mixture is required here to follow the argument further.

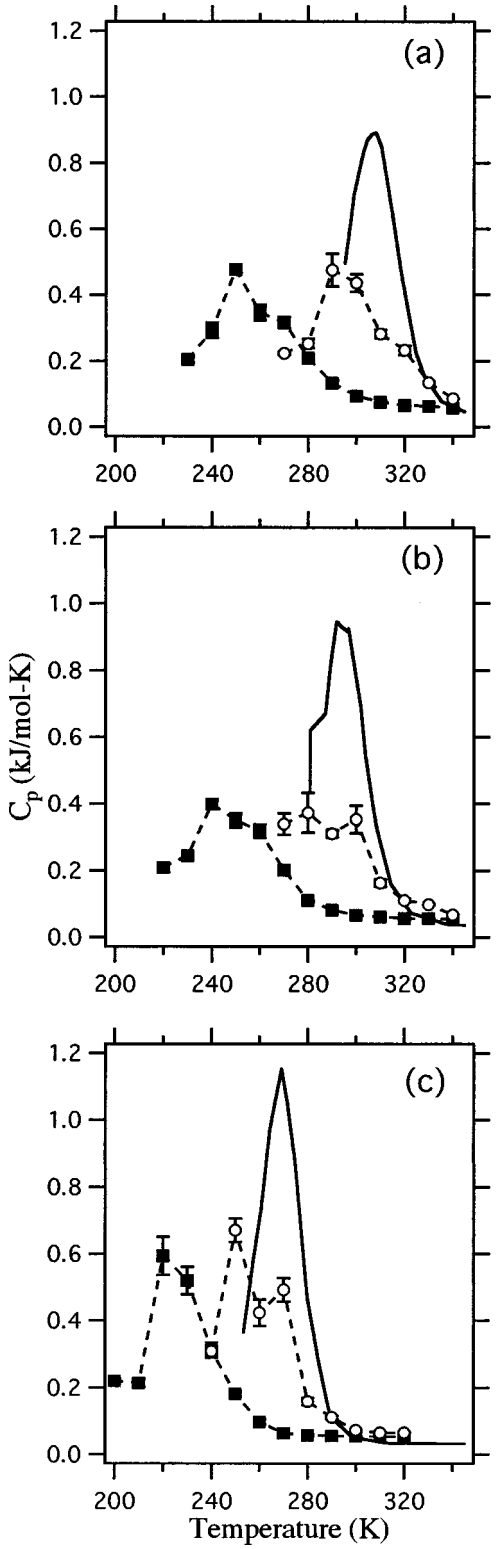

FIG. 9. The heat capacity of the superheated vapor along three isobars: 96.1 kPa (a); 56.0 kPa (b); and 15.5 kPa (c), as calculated from biased NPT simulations of the BH82 model (filled squares) and the CJ84 model (open circles) with the experimental data of Ref. 48 (solid line). The broken lines connecting the symbols are drawn as guides for the eye. Error bars are shown only when larger than the plotting symbol.

Without any knowledge of association, the pure component molar heat capacity at constant pressure is written as

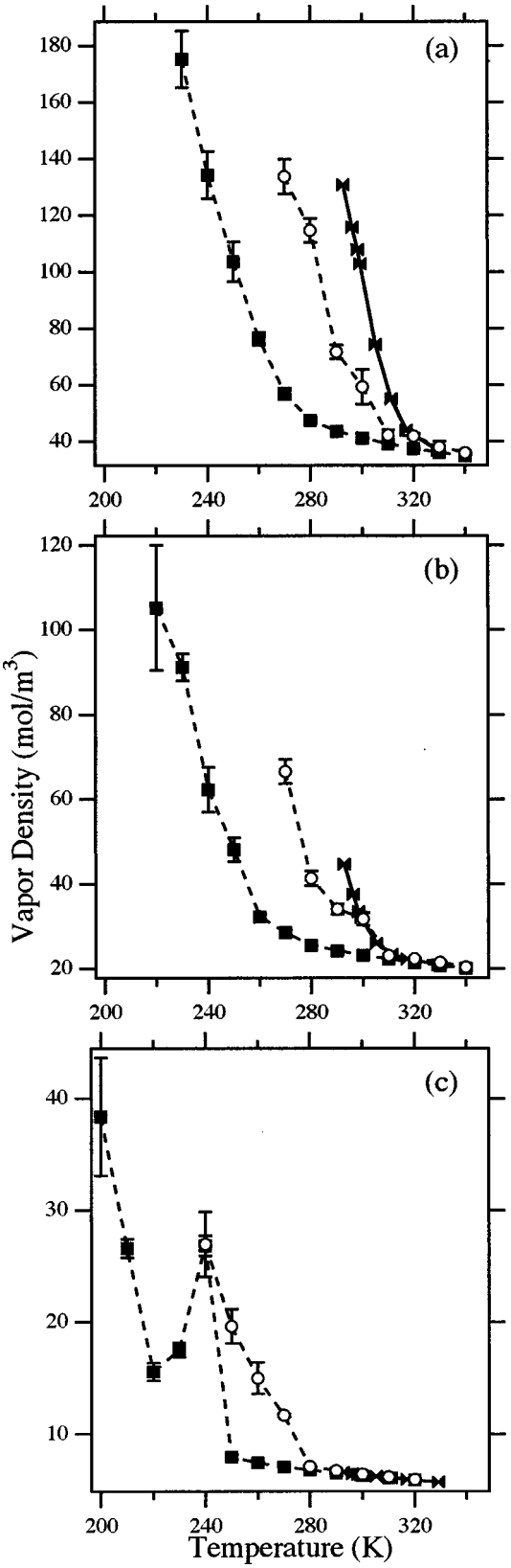

FIG. 10. The superheated vapor density along three isobars, 96.1 kPa (a); 56.0 kPa (b); and 15.5 kPa (c), as calculated from biased NPT simulations of the BH82 model (filled squares) and the CJ84 model (open circles) with the experimental data of Ref. 46 (solid bow ties). The broken lines connecting the symbols are drawn as guides for the eye.

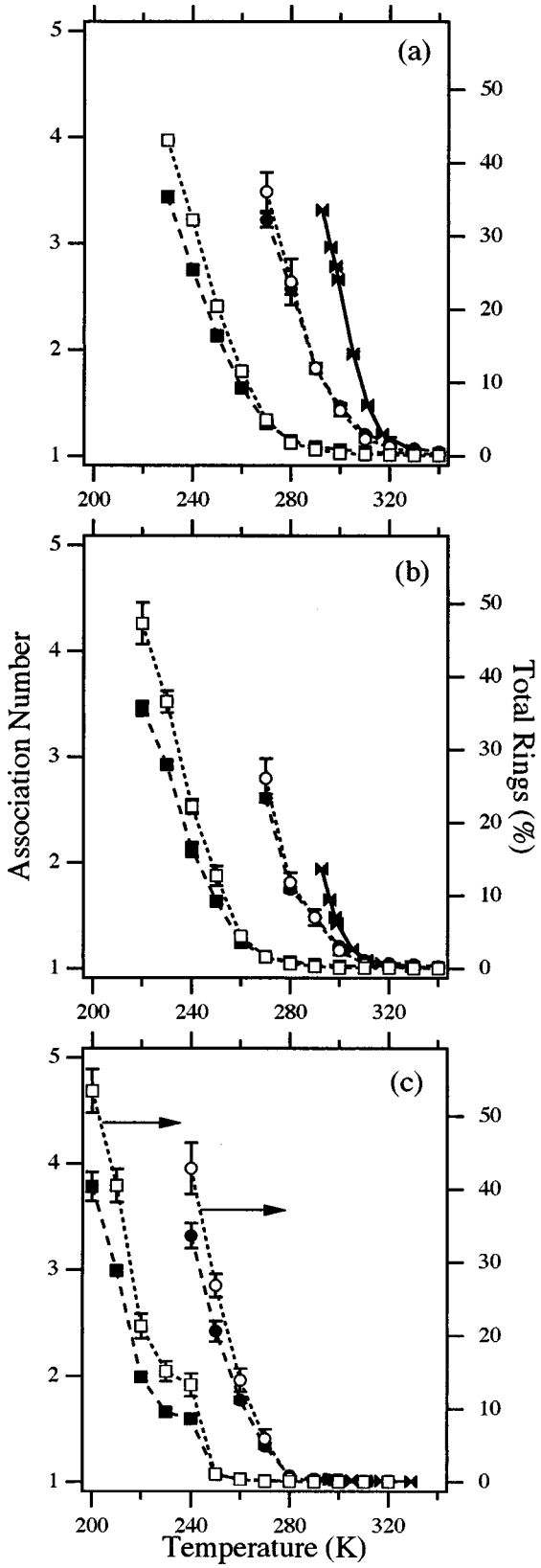

FIG. 11. The association number (filled symbols, left axis) and percentage of rings (open symbols, right axis) along three isobars: 96.1 kPa (a); 56.0 kPa (b); and 15.5 kPa (c), as calculated from biased NPT simulations of the BH82 model (squares) and the CJ84 model (circles) with the experimental data of Ref. 46 (solid bow ties). The broken lines connecting the symbols are drawn as guides for the eye.

TABLE III. Relevant properties from simulation and experiment at the heat capacity peak for the 96.1 kPa isobar.

	C_p peak temp. K	χ	$(\partial\chi/\partial T)_P$ K^{-1}
Expt.	305	1.96	−0.098
BH82	250	2.13	−0.058
CJ84	290	1.82	−0.058

$$C_p=\left(\frac{\partial h}{\partial T}\right)_P, \tag{3}$$

where h is the apparent molar enthalpy. For a mixture, this becomes

$$C_p=\frac{1}{N_{\text{app}}}\sum_{i=1}^{\infty}\left(\frac{\partial(N_iH_i)}{\partial T}\right)_P, \tag{4}$$

where N_{app} is the apparent number of moles, N_i is the number of moles of species i, and H_i is the partial molar enthalpy of species i.[49] If we assume that the partial molar enthalpy is a function only of the number of hydrogen bonds, we can write $H_1=0$, and $H_i=(i-1)H_2$ for all higher species, assuming only straight chains. Thus, Eq. (4) becomes

$$\begin{aligned}C_p=(1/N_{\text{app}})&\left[N_2\left(\frac{\partial H_2}{\partial T}\right)_P+2N_3\left(\frac{\partial H_2}{\partial T}\right)_P\right.\\&\left.+3N_4\left(\frac{\partial H_2}{\partial T}\right)_P+\cdots\right]+(1/N_{\text{app}})\left[H_2\left(\frac{\partial N_2}{\partial T}\right)_P\right.\\&\left.+H_2\left(\frac{\partial(2N_3)}{\partial T}\right)_P+H_2\left(\frac{\partial(3N_4)}{\partial T}\right)_P+\cdots\right],\end{aligned} \tag{5}$$

$$\begin{aligned}C_p=&\left(\frac{\partial H_2}{\partial T}\right)_P(1/N_{\text{app}})\left(\sum_{i=1}^{\infty}iN_i-\sum_{i=1}^{\infty}N_i\right)\\&+(H_2)(1/N_{\text{app}})\frac{\partial}{\partial T}\left(\sum_{i=1}^{\infty}iN_i-\sum_{i=1}^{\infty}N_i\right)_P.\end{aligned} \tag{6}$$

If we utilize the definition of the association number χ, Eq. (6) can be written as

$$C_p=\left(\frac{\partial H_2}{\partial T}\right)_P\left(1-\frac{1}{\chi}\right)-H_2\frac{\partial}{\partial T}\left(\frac{1}{\chi}\right)_P, \tag{7}$$

which is written more conveniently as

$$C_p=\left(\frac{\partial H_2}{\partial T}\right)_P\left(1-\frac{1}{\chi}\right)+(H_2/\chi^2)\left(\frac{\partial\chi}{\partial T}\right)_P. \tag{8}$$

From the above it is clear that the heat capacity for associating systems can be examined as the sum of two terms: the first term is a ''conventional'' heat capacity which measures the rate of change of an enthalpy with temperature, while the second term looks at the rate of change of the association number with temperature. Thus, it is not enough to predict an accurate association number to get correct heat capacity behavior; good representation of how the association number varies with temperature is required as well. We can see from Table III that both potential models predict the same temperature derivative for the association number at the heat capacity peak temperature; both are about half that of the experiment. A better match with the experiment for this term would move the magnitude of the predicted heat capacity peak in the simulation studies towards that found by the experiment. Of course this simple qualitative argument is made only to illustrate the importance of the association number and its temperature derivative in predicting a correct heat capacity. The true dependence of C_p on χ and $\partial\chi/\partial T$ is more complex than given from our argument (for example, distinctions between a ring and a chain of the same length complicates matters).

It is interesting to look at the various oligomer distributions predicted by both models over the range of temperatures and pressures simulated. The main difference between the models is that the effective potential has implicitly included greater than pair interactions, so a comparison of the models would give some insight into how these 3+ body effects influence cluster formation.

Returning to Fig. 11, it is seen that both models predict a large degree of ring formation at similar states, if we allow for a temperature translation to better compare the models. In Fig. 12 (chains) and Fig. 13 (rings) we give a more detailed look at the distributions obtained for the relevant species in the CJ84 potential model along the three isobars simulated. From these figures, it is clear that the monomer and the ring tetramer are the most important mixture components, the latter falling quickly to zero mole fraction at near-ideal gas states. Other species, such as the ring pentamer and chain tetramer and dimer are also important at some states. The dimer actually shows a peak indicating that it is an intermediate species in the decomposition of larger clusters. In Fig. 14 (chains) and Fig. 15 (rings) we look at the distributions predicted by the BH82 potential model. Conclusions similar to the CJ84 model regarding the species' importance can also be made from the BH82 model. Also, the peak in the dimer distribution is more enhanced in the BH82 model than the CJ84 model. Additionally, the relative amount of ring tetramer is much larger in this model than in the effective potential. This indicates that the 3+ body interactions are repulsive; the absence of this repulsion in the BH82 model allows more of the tetramer to form. It is interesting to note that these results indicate that the ring pentamer is a relevant species while the hexamer, long included in most association schemes attached to equations of state, is nearly negligible in both forms at most states.

V. CONCLUSION

We have presented the VLE, vapor pressure, and heat of vaporization for HF from MC simulation of three potential models, one of which was an effective potential. The effective potential was simple and provided the best results, relative to experiment, of the three models tested. We also developed a biasing algorithm and determined the constant-pressure heat capacity of HF in the superheated vapor state from nonbiased and biased NPT simulations at 96.1 kPa as a function of temperature for the effective potential. We determined the heat capacity along this isobar and two others as a

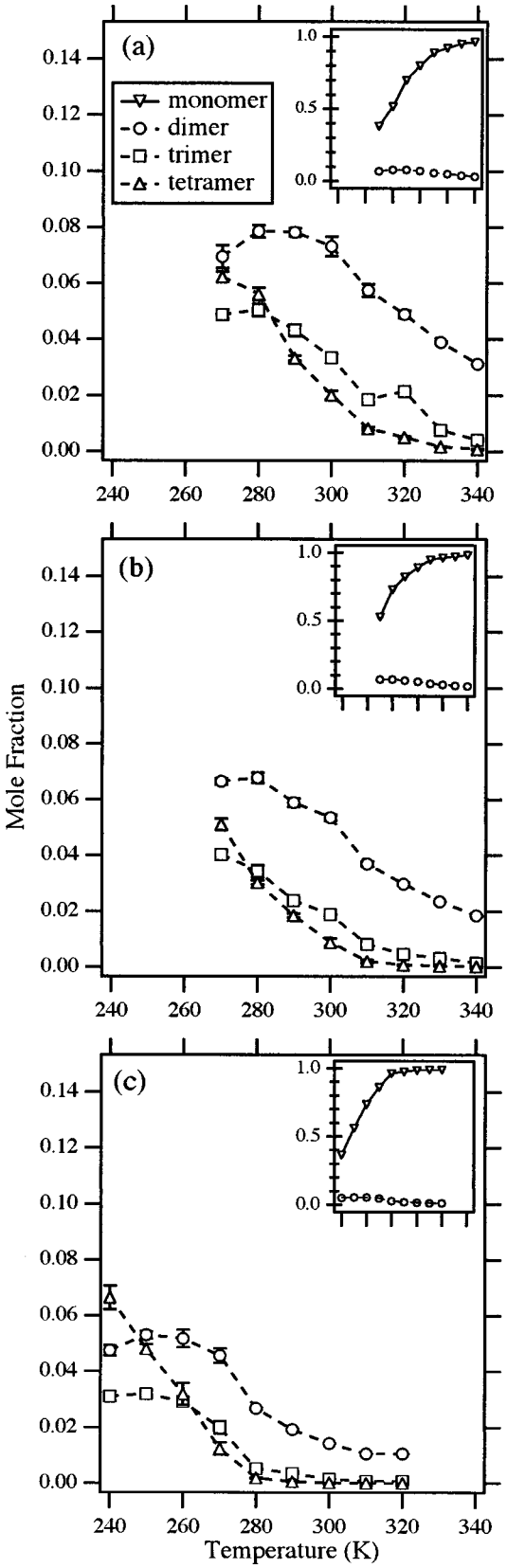

FIG. 12. The oligomer distribution for relevant chain species along three isobars: 96.1 kPa (a); 56.0 kPa (b); and 15.5 kPa (c), as calculated from biased NPT simulations of the CJ84 model. The inset compares the monomer mole fraction to the dimer mole fraction. The horizontal scale of the inset is the same as the figure enclosing it.

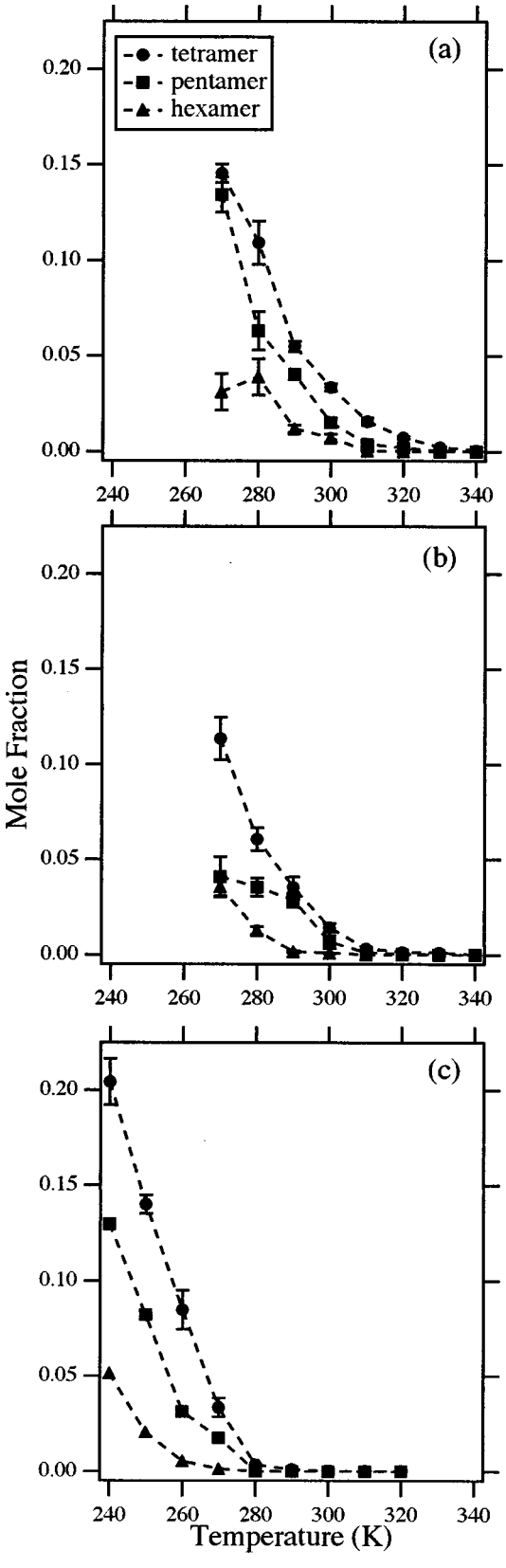

FIG. 13. The oligomer distribution for relevant ring species along three isobars: 96.1 kPa (a), 56.0 kPa (b), and 15.5 kPa (c), as calculated from biased NPT simulations of the CJ84 model.

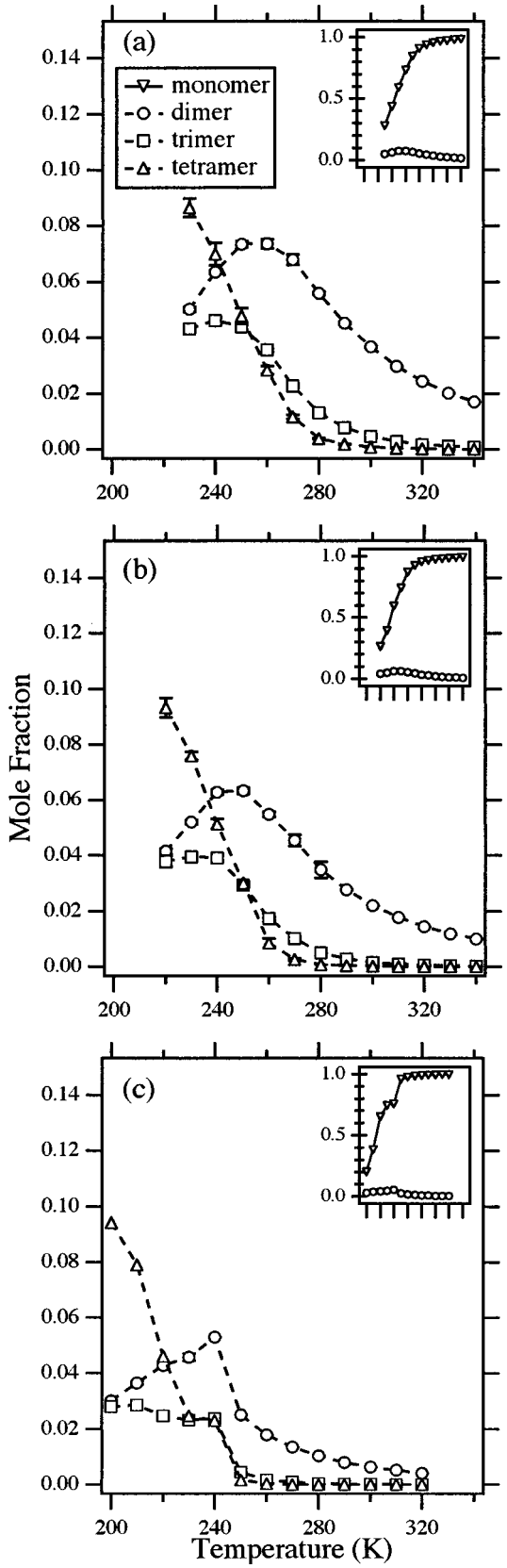

FIG. 14. The oligomer distribution for relevant chain species along three isobars: 96.1 kPa (a), 56.0 kPa (b), and 15.5 kPa (c), as calculated from biased NPT simulations of the BH82 model. The inset compares the monomer mole fraction to the dimer mole fraction. The horizontal scale of the inset is the same as the figure enclosing it.

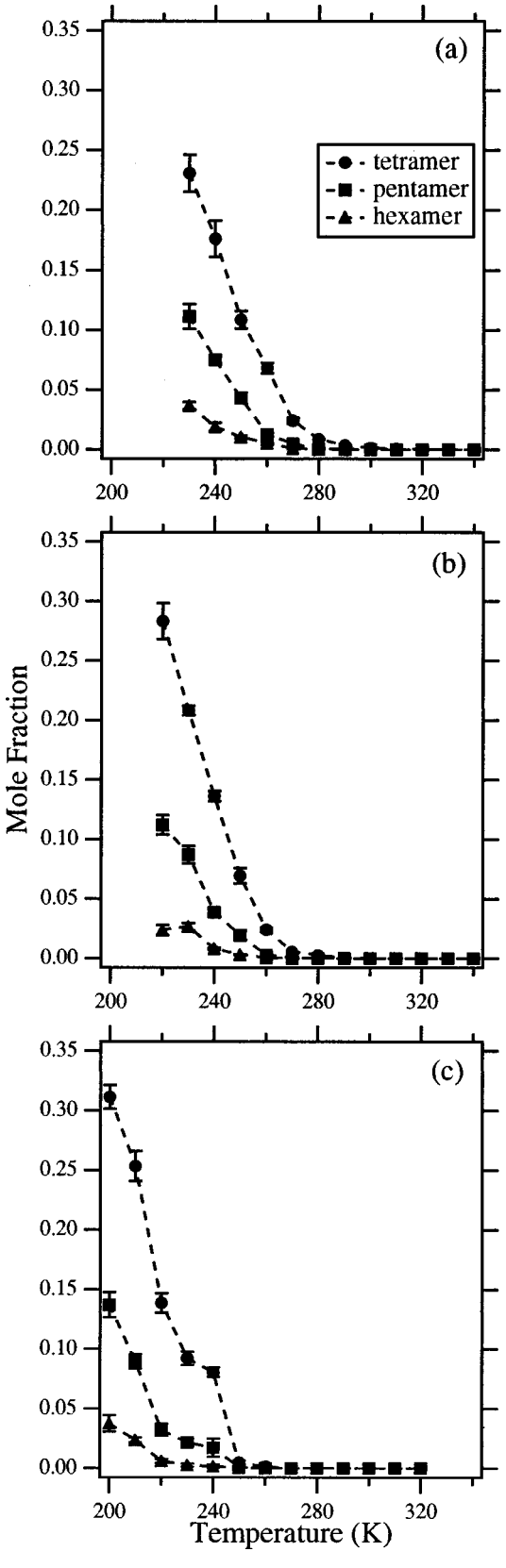

FIG. 15. The oligomer distribution for relevant ring species along three isobars: 96.1 kPa (a), 56.0 kPa (b), and 15.5 kPa (c), as calculated from biased NPT simulations of the BH82 model.

function of temperature using the biased NPT simulations for the effective and semi-empirical pair potentials. The NPT simulations for both models showed a peak in the heat capacity as a function of temperature but the peaks were much smaller and occurred at lower temperatures relative to published experimental data for HF.

From our biased NPT simulations we were able to extract information about the density, degree of association, and the composition of the superheated vapor at all the states simulated. The results indicated that both potential models predict less association and a lower density than experiment. It was found that the percentage of rings in the vapor was very substantial for both models at low temperatures but quickly decreased as the temperature increased. Also, the ring tetramer is the important oligomer other than the monomer, which is consistent with the findings of other workers.[32,33,50] Although the ring pentamer is often discounted in much modeling work we found it to be not negligible, a finding which corroborates Quack *et al.*'s assertion of its importance.[18] Also, the hexamer was found to be unimportant at most states.

From our work, we can conclude that a useful association scheme for HF in the vapor phase would include, at most, the seven relevant species: monomer, dimer (chain), trimer (chain), tetramer (chain and ring), pentamer (ring), and hexamer (ring). Future work could include the use of this association scheme in modifying existing equations with specifications that distinguish between a chain and a ring. We would also like to look at a recent dimer PES that includes higher order corrections,[51,52] and potentials with explicit three-body forces.

ACKNOWLEDGMENTS

Acknowledgment is made to the Donors of the Petroleum Research Fund, administered by the American Chemical Society, for partial support of this research. Additional support was provided by the National Science Foundation. Both authors would like to thank H. F. King, J. Gao, R. E. Stanton, and T. Furlani for insightful discussions into this work.

APPENDIX

The complicated nature of the BH82 potential makes the calculation of the pressure via the virial demanding. Thus, a method very similar to that proposed by Harismiadis *et al.*[53] which built on earlier work of Eppenga and Frenkel[54] is used. Note that the validity of this method was checked by calculating the pressures for the other potentials studied in this work (J79 and CJ84) via this method. The pressures calculated this way compared favorably (within ± 1 atm) to the pressures calculated from the virial.

A useful equation which approximates the pressure in the GE is

$$\beta P = (1/\Delta V)\ln\left\langle \left(\frac{V'}{V}\right)^N \exp(-\beta \Delta U)\right\rangle, \tag{A1}$$

where P is the pressure, β is the reciprocal temperature, V is the volume of state i, V' is the volume of state j, $\Delta V = V' - V$, ΔU is the energy change in going from state i to state j, N is the number of particles in the phase of interest, and the $\langle \cdots \rangle$ signifies an ensemble average. We will also give the symbol Y to represent the argument of the logarithm in the above equation. The above equation is accurate only for small ΔV and is utilized by Harismiadis *et al.* with a fixed ΔV. We propose a similar method which will loosen up the restriction of fixed ΔV and allow us to adhere better to the goal of a small ΔV when implementing the equation.

During the simulation, we create a histogram of Y as a function of the ΔV chosen randomly along $(-\Delta V_{\max}, +\Delta V_{\max})$, where the bin increments were 1 Å^3. We then fit the logarithm of Y for each bin divided by the ΔV of that bin to a quadratic in ΔV. The zeroth degree constant of the quadratic determines the pressure. The corresponding statistical error in the average pressure comes from the errors in the average of Y for each bin, propagated into an error in the constants of the quadratic.

[1] E. Chung and M. Kim, J. Chem. Eng. Data **42**, 1126 (1997).
[2] O. Tsvetkov, Y. A. Laptev, and A. Asambaev, Int. J. Thermophys. **15**, 203 (1994).
[3] M. Nagel and K. Bier, Int. J. Refrig. **18**, 534 (1995).
[4] G. Matthews, D. Dowdell, and I. Wells, J. Phys. D **30**, 2012 (1997).
[5] D. Defibaugh and G. Morrison, Fluid Phase Equilibria **80**, 157 (1992).
[6] L. Weber, Fluid Phase Equilibria **80**, 141 (1992).
[7] Y. Ikeya, C. Piao, H. Sato, and K. Watanabe, Fluid Phase Equilibria **80**, 119 (1992).
[8] I. Economou, C. Peters, L. Florusse, and J. D. S. Arons, Fluid Phase Equilibria **111**, 239 (1995).
[9] J. Lee, H. Kim, J. S. Lim, J. D. Kim, and Y. Y. Lee, J. Chem. Eng. Data **41**, 43 (1996).
[10] M. Lencka and A. Anderko, AIChE. J. **39**, 533 (1993).
[11] C. H. Twu, J. E. Coon, and J. R. Cunningham, Fluid Phase Equilibria **86**, 47 (1993).
[12] C. P. C. Kao, M. E. Paulaitis, G. A. Sweany, and M. Yokozeki, Fluid Phase Equilibria **108**, 27 (1995).
[13] I. Economou and C. Peters, Ind. Eng. Chem. Res. **34**, 1868 (1995).
[14] A. Galindo, P. Whitehead, G. Jackson, and A. Burgess, J. Phys. Chem. B **101**, 2082 (1997).
[15] D. F. Smith, J. Chem. Phys. **28**, 1040 (1958).
[16] J. Janzen and L. Bartell, J. Chem. Phys. **50**, 3611 (1969).
[17] L. A. Curtiss and M. Blander, Chem. Rev. **88**, 827 (1988).
[18] M. Quack, U. Schmitt, and M. A. Suhm, Chem. Phys. Lett. **208**, 446 (1993).
[19] W. G. Chapman, K. Gubbins, G. Jackson, and M. Radosz, Fluid Phase Equilibria **52**, 31 (1989).
[20] D. Visco, Jr. and D. Kofke, Fluid Phase Equilibria (submitted).
[21] M. L. Klein, I. R. McDonald, and S. F. O'Shea, J. Chem. Phys. **69**, 63 (1978).
[22] K. Honda, K. Kitaura, and K. Nishimoto, Bull. Chem. Soc. Jpn. **65**, 3122 (1992).
[23] W. L. Jorgensen, J. Chem. Phys. **70**, 5888 (1979).
[24] A. E. Barton and B. J. Howard, Faraday Discuss. Chem. Soc. **73**, 45 (1982).
[25] M. L. Klein and I. R. McDonald, J. Chem. Phys. **71**, 298 (1979).
[26] M. E. Cournoyer and W. L. Jorgensen, Mol. Phys. **51**, 119 (1984).
[27] S. Murad, K. A. Mansour, and J. G. Powles, Chem. Phys. Lett. **131**, 98 (1986).
[28] P. Jedlovszky and R. Vallauri, J. Chem. Phys. **107**, 10166 (1997).
[29] P. Jedlovszky and R. Vallauri, Mol. Phys. **92**, 331 (1997).
[30] U. Rothlisberger and M. Parrinello, J. Chem. Phys. **106**, 4658 (1997).
[31] K. Laasonen and M. Klein, Mol. Phys. **88**, 135 (1996).
[32] C. Zhang, D. L. Freeman, and J. D. Doll, J. Chem. Phys. **91**, 2489 (1989).
[33] H. Sun, R. O. Watts, and U. Buck, J. Chem. Phys. **96**, 1810 (1992).
[34] M. P. Allen and D. J. Tildesley, *Computer Simulation of Liquids* (Oxford, New York, 1994).
[35] D. Yarkony, S. O'Neill, H. Schaefer III, C. Baskin, and C. Bender, J. Chem. Phys. **60**, 855 (1974).

[36] G. Maitland, M. Rigby, E. Smith, and W. Wakeham, *Intermolecular Forces* (Clarendon, New York, 1987).
[37] D. A. Kofke, J. Chem. Phys. **98**, 4149 (1993).
[38] A. Z. Panagiotopoulos, Mol. Phys. **61**, 813 (1987).
[39] F. Bresme, E. Lomb, and J. L. F. Abascal, J. Chem. Phys. **106**, 1569 (1997).
[40] N. A. Busch, M. S. Wertheim, and M. L. Yarmush, J. Chem. Phys. **104**, 3962 (1996).
[41] D. M. Tsangaris and J. J. dePablo, J. Chem. Phys. **101**, 1477 (1994).
[42] M. Suhm, Ber. Bunsenges. Phys. Chem. **99**, 1159 (1995).
[43] E. U. Franck and W. Spalthoff, Z. Elektrochem. **61**, 348 (1957).
[44] I. Sheft, A. J. Perkins, and H. H. Hyman, J. Inorg. Nucl. Chem. **35**, 3677 (1973).
[45] J. H. Simons and J. W. Bouknight, J. Am. Chem. Soc. **54**, 129 (1932).
[46] C. E. Vanderzee and W. W. Rodenberg, J. Chem. Thermodyn. **2**, 461 (1970).
[47] K. Fredenhagen, Z. Anorg. Allg. Chem. **218**, 161 (1934).
[48] E. U. Franck and F. Meyer, Z. Elektrochem. **63**, 571 (1959).
[49] R. Redington, J. Phys. Chem. **86**, 552 (1982).
[50] M. Quack, J. Stohner, and M. A. Suhm, J. Mol. Struct. **294**, 33 (1993).
[51] M. Quack and M. A. Suhm, J. Chem. Phys. **95**, 28 (1991).
[52] M. Quack and M. A. Suhm, *Conceptual Trends in Quantum Chemistry* (Kluwer, Dordrecht, 1997), Vol. III.
[53] V. I. Harismiadis, J. Vorholz, and A. Z. Panagiotopoulos, J. Chem. Phys. **105**, 8469 (1996).
[54] R. Eppenga and D. Frenkel, Mol. Phys. **52**, 1303 (1984).